Electronic Supplementary Material (ESI) for ChemComm.

Electronic Supporting Information

Flexible and Stable Copper-Based Halide Scintillators for High-Performance X-Ray Imaging

Baiqian Wang,†[a] Zhenglin Jia,†[b] Xin Yang,†[a] Shirong Lu,[c] Jinrong Zhao,[a] Zhe Sun,[a] Qingkai Qian,[a,] Qianqian Lin[b,*] and Zhigang Zang[a,*]*

[a]Key Laboratory of Optoelectronic Technology & Systems (Ministry of Education), Chongqing University, Chongqing, 400044, China

[b]School of Physics and Technology, Wuhan University, Wuhan, 430072, China

[c]Department of Material Science and Technology, Taizhou University, Taizhou, 318000, China

E-mail: qqian@cqu.edu.cn, q.lin@whu.edu.cn, zangzg@cqu.edu.cn

METHODS

Chemical Preparations. Copper bromide (CuBr, 99.9%), rubidium carbonate (Rb_2CO_3, 99.9%), and n-hexane (97%) were purchased from Macklin Co., Ltd. 1-Octadecene (>90%), oleylamine (>90%), oleic acid (97%), and toluene (99.5%) were purchased from Aladdin Co. Ltd. Polymethyl methacrylate (PMMA, >98%) was purchased from Tokyo Co. Ltd.

Synthesis of Rb_2CuBr_3 NCs. Rb_2CuBr_3 NCs were synthesized using a hot-injection method, in which raw materials of CuBr (0.172 g) are dissolved in solution 1-octadecene (20 ml) together with oleylamine (2 ml) and oleic acid (2 ml). Then, the above mixture was heated to 170 °C at N_2 atmosphere. Finally, the nucleation and growth of Rb_2CuBr_3 NCs was triggered by the rapid injection of Rb-oleate (4 ml). After 10 s, the above raw mixture was quenched to room temperature, and the Rb_2CuBr_3 NCs were purified by centrifugation (8000 rpm for 5 min) with n-hexane. The above Rb-oleate was obtained by dissolving Rb_2CO_3 (0.231 g) in 1-octadecene (5 ml) and oleic acid (1.5 ml), with 140 °C at N_2 atmosphere.

Synthesis of polymer films. PMMA (1200 mg) powders were added into toluene (8 ml) and stirred at 50 °C for 1 hour. Then, the PMMA colloids were added into the as-synthesized Rb_2CuBr_3 NCs and stirred at atmospheric environment for one more hour. The above mixture of Rb_2CuBr_3 NCs@PMMA colloid was removed into the prefabricated template and heated in air. The flexible film of $CsPbBr_3$@PMMA can be peeled off. The thickness of the films was controlled by the mixture amount added to the template.

DFT calculations. DFT calculations are conducted using Vienna ab initio simulation package (VASP). Density functional of Perdew-Burke-Ernzerhof (PBE) with generalized gradient approximation (GGA) was used. Projector augmented wave (PAW) pseudopotential was adopted. The kinetic cutoff energy was set to be 400 eV. The electronic wavefunction was self-consistently converged to 10^{-5} eV. During the lattice relaxation, Gamma-center k-point mesh grids of 6×2×2 and atomic force criteria of 0.005 eV/Å were used. To further correct the

bandgap, hybrid functional of HSE06 was used, and the band structure and DOS were interpolated by the maximally localized Wannier functions (MLWFs) through Wannier90 codes. To simulate the self-trapped exciton effect, one spin-down electron in the collinear spin-polarized calculation was excited to the lowest unoccupied spin-up or spin-down conduction band, and then the atomic structure was relaxed again while maintaining the band occupations.

Characterizations. XRD measurements were conducted using a Cu Kα X-ray tube (40 kV, 40 mA) by PANalytical X'Pert Powder (Spectris Pte. Ltd., Netherlands). XPS spectra were performed by ESCALAB250Xi (Thermo Fisher Scientific Co., Ltd., USA). TEM measurements were measured by Talos F200S (Thermo Fisher Scientific Co., Ltd., USA). Both PLE and PL characterizations were performed in air environment. The steady and transient PL of Rb_2CuBr_3 NCs were measured using fluorescence spectrometer (FLS1000, Edinburgh Instruments Ltd., England). The total X-ray attenuation rate of the Rb_2CuBr_3 can be obtained from the XCOM: Photon Cross Sections Database (NIST Standard Reference Database 8, 2013). For the RL and X-ray imaging measurements, a commercial X-ray source L10321 (Hamamatsu Co., Ltd., Japan) was used. The RL spectra and X-ray detection limit were recorded by NOVA-EX fiber optic spectrometer (Shanghai Ideaoptics Co., Ltd., China) and SM1PD2A photodetector (Changchun ocean electro-optics Co., Ltd., China). The X-ray scintillation image was captured by Charge-coupled device (CCD, KAF-16803, USA).

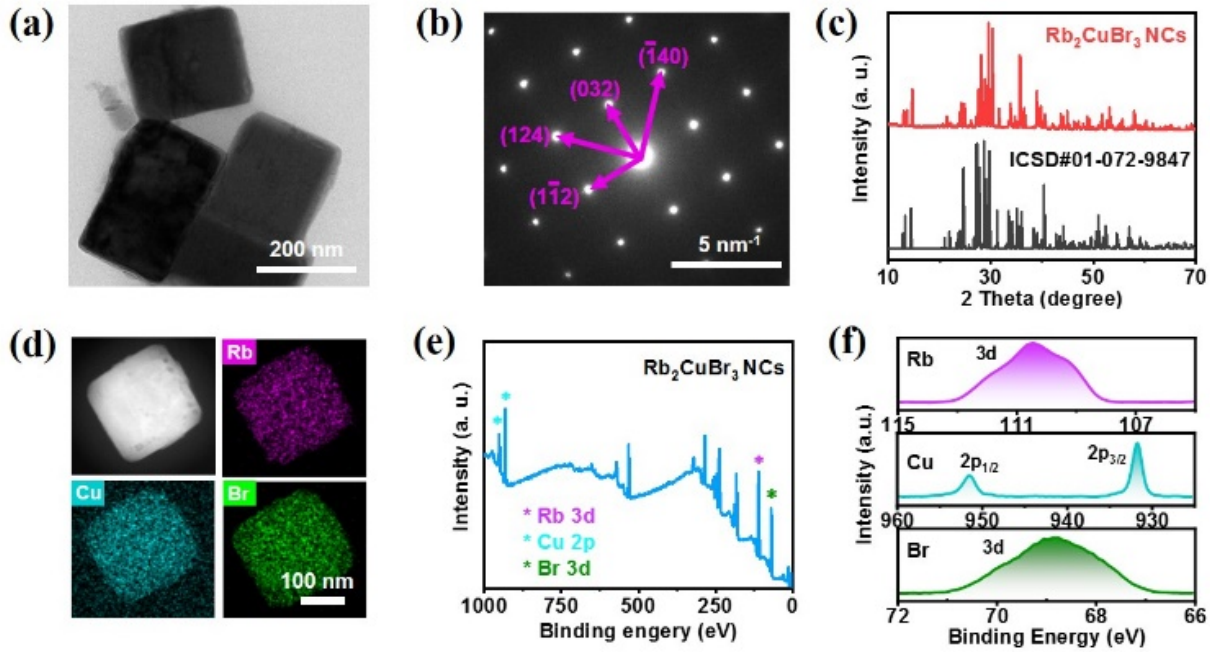

Figure S1. (a) Transmission electron microscope (TEM) image, (b) electron diffraction pattern and (c) X-ray diffraction (XRD) patterns of Rb_2CuBr_3 NCs. (d) Energy dispersive X-ray (EDX) mapping of Rb, Cu, and Br elements. (e) Survey spectrum of X-ray photoelectron spectroscopy (XPS) and (f) the enlarged spectra of Rb, Cu, and Br. Especially, the XPS peak of Cu $2p_{3/2}$ is located at 932.5 eV and fitted well with a Gaussian function, indicating the univalent Cu with the absence of Cu^{2+}.

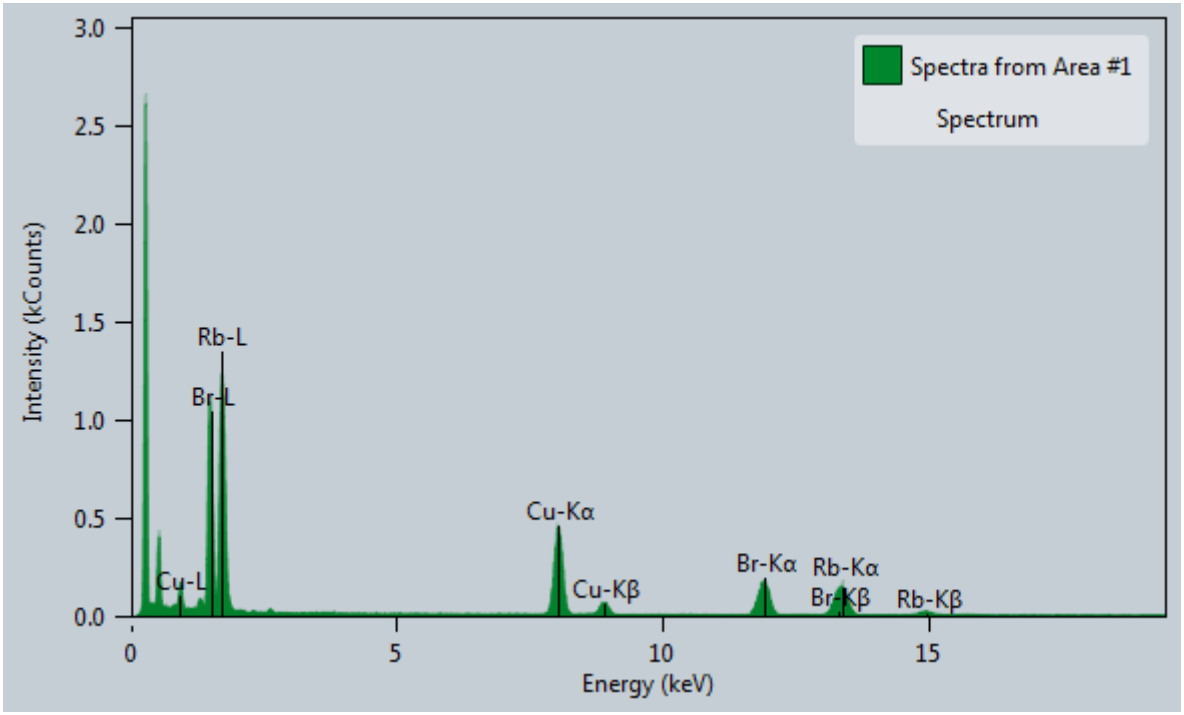

Figure S2. Energy-dispersive X-ray spectroscopy of Rb_2CuBr_3 NCs.

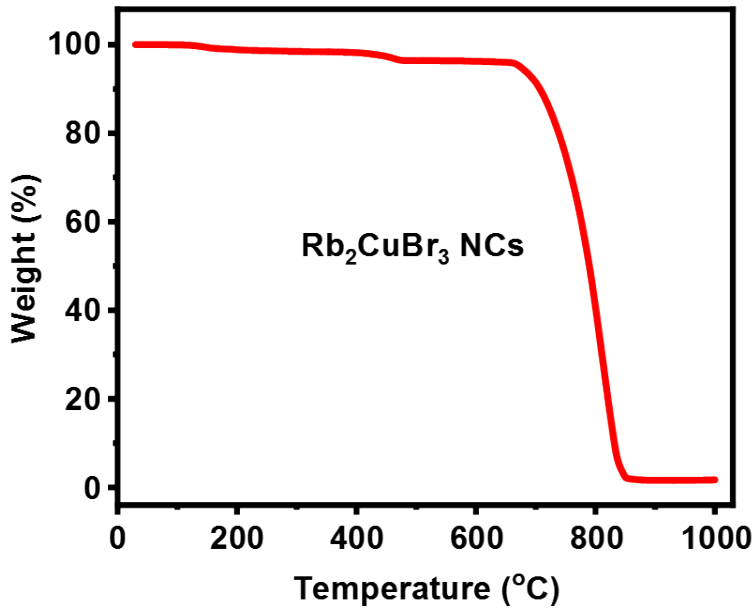

Figure S3. Thermogravimetric curve of Rb_2CuBr_3 NCs.

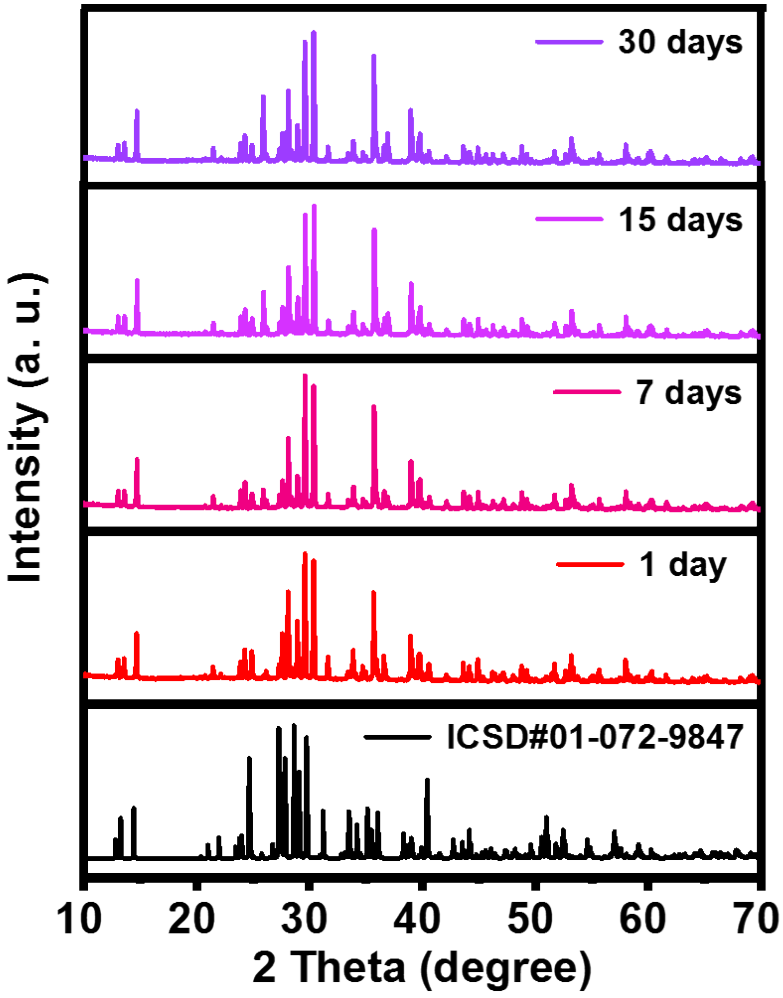

Figure S4. XRD patterns of Rb_2CuBr_3 NCs stored in air for different time.

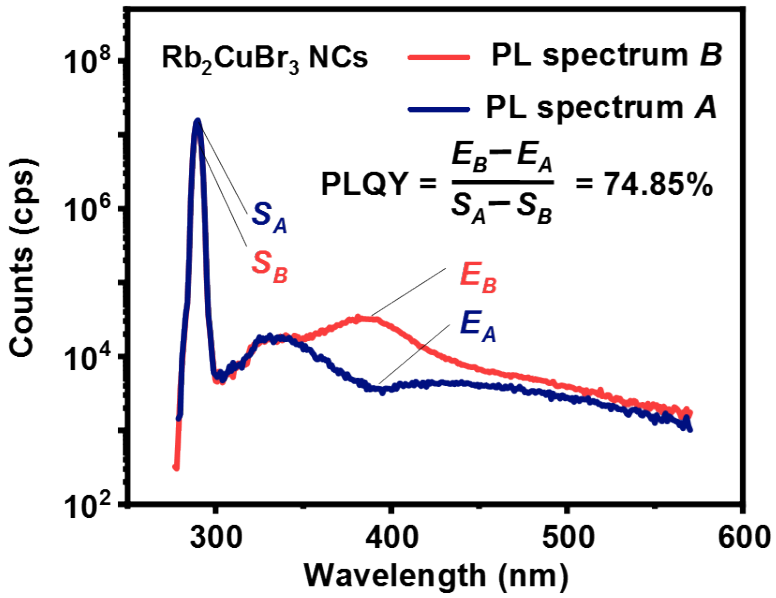

Figure S5. PLQY of Rb_2CuBr_3 NCs. PL spectrum A and B are for blank sample and Rb_2CuBr_3 NCs respectively, measured in an integrated sphere. S_A and S_B are intensities for photons at excitation wavelength, while E_A and E_B are intensities for photons of PL emission.

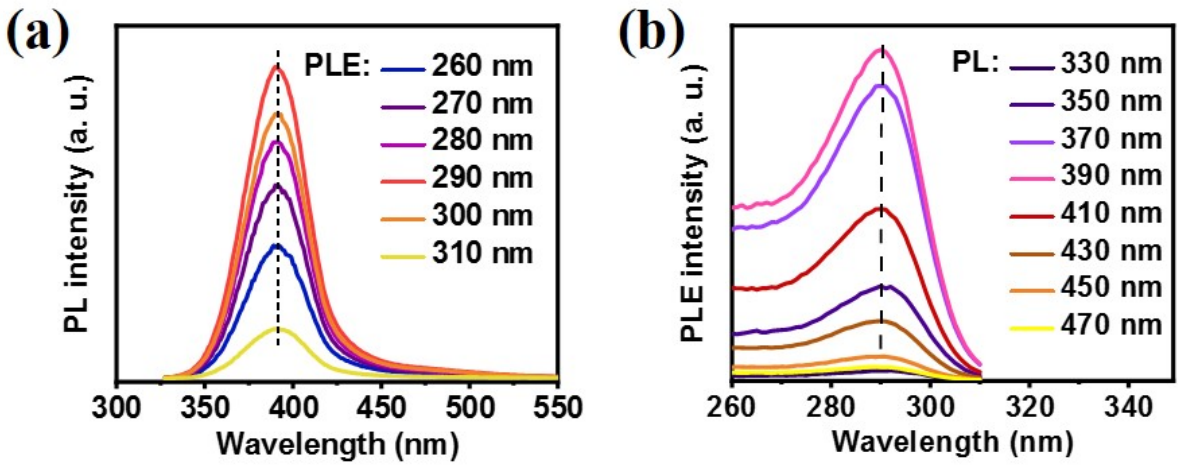

Figure S6. (a) PL spectra under different wavelength excitations. (b) Emission-wavelength dependent PL excitation (PLE) spectra of Rb_2CuBr_3 NCs.

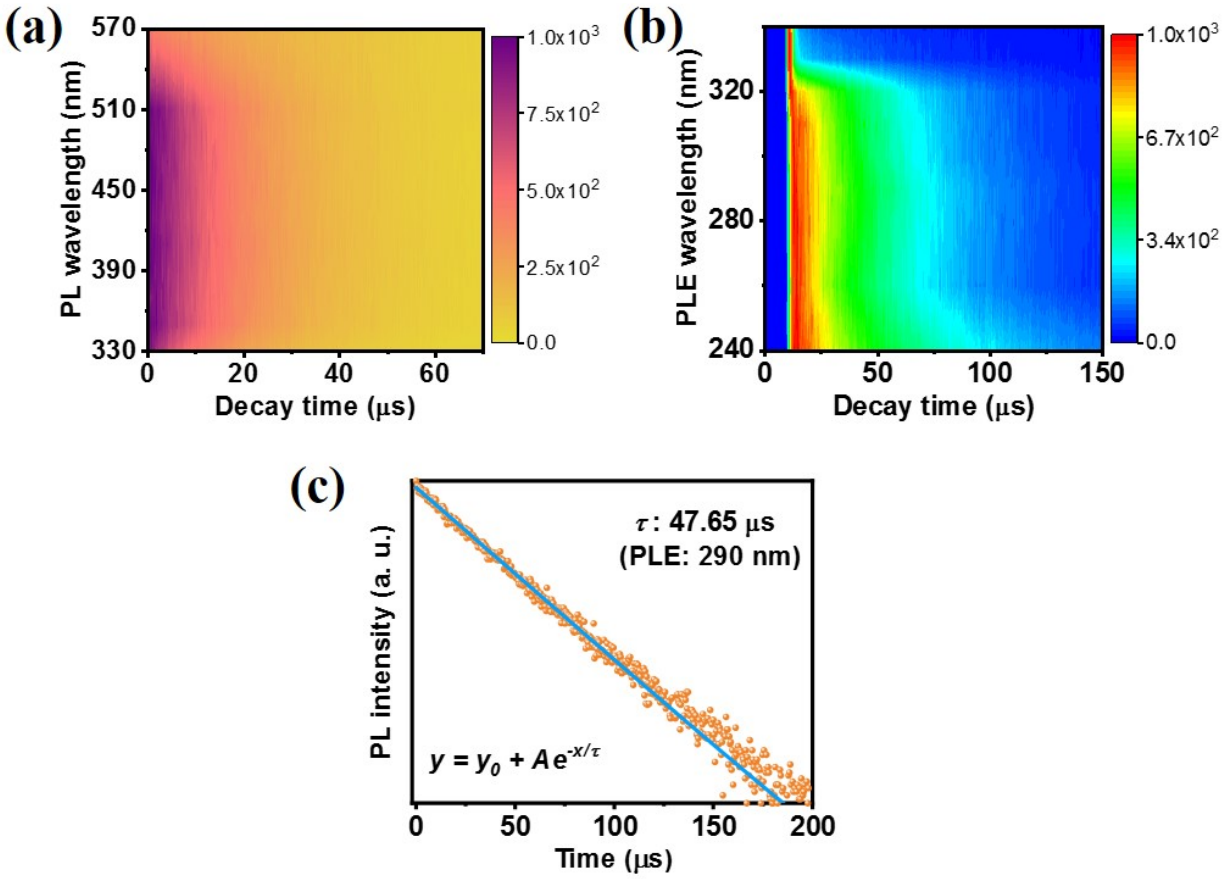

Figure S7. (a) Transient PL mapping after 290 nm pulse excitation. (b) The emission-wavelength dependent PLE spectra of Rb_2CuBr_3 NCs with different decay time (Monitored PL peak at 390 nm). (c) Time-resolved PL decay curve and fitting lifetime of Rb_2CuBr_3 NCs.

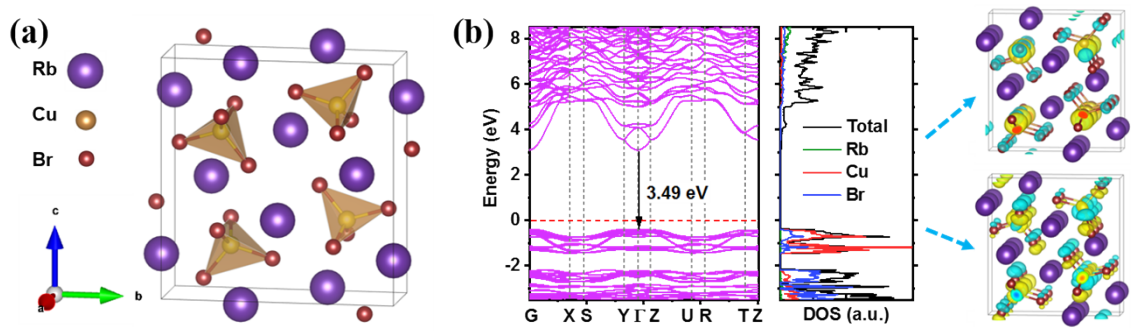

Figure S8. (a) Crystal structure of Rb_2CuBr_3 and (b) the corresponding electronic band diagram, density of states (DOS), and electron wavefunctions at conduction band minimum (CBM) and valence band maxmimum (VBM).

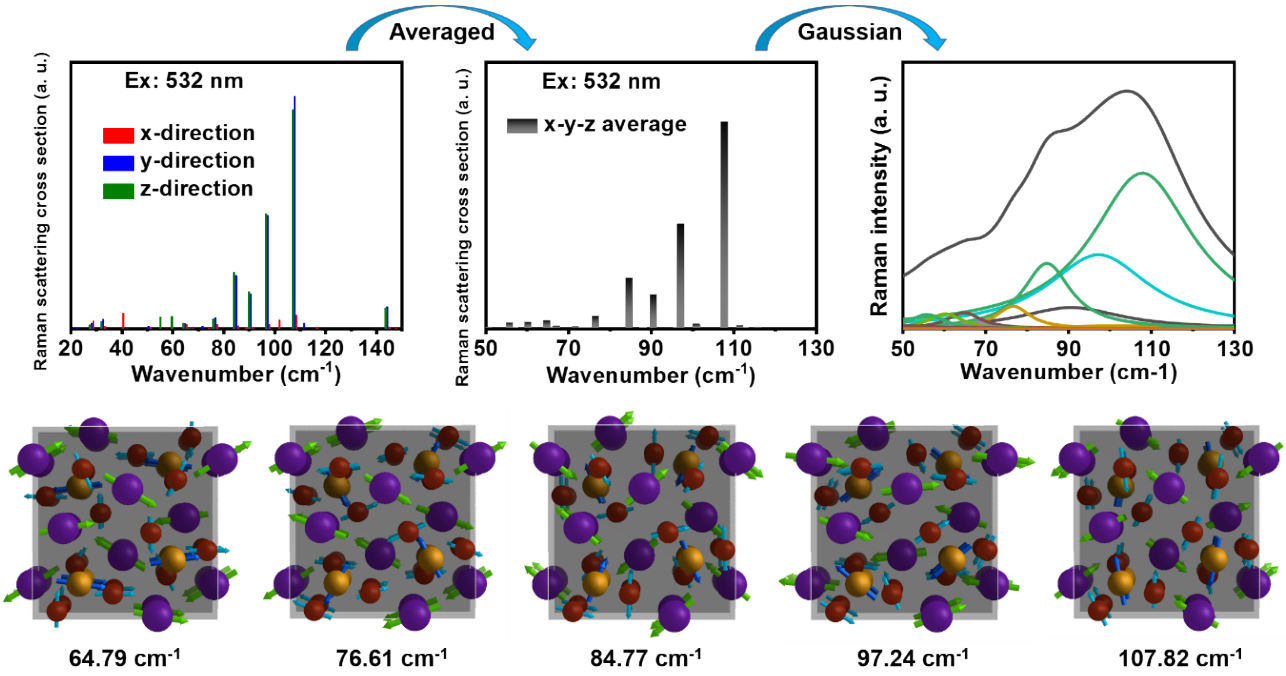

Figure S9. Calculated Raman spectra and typical phonon modes of Rb_2CuBr_3.

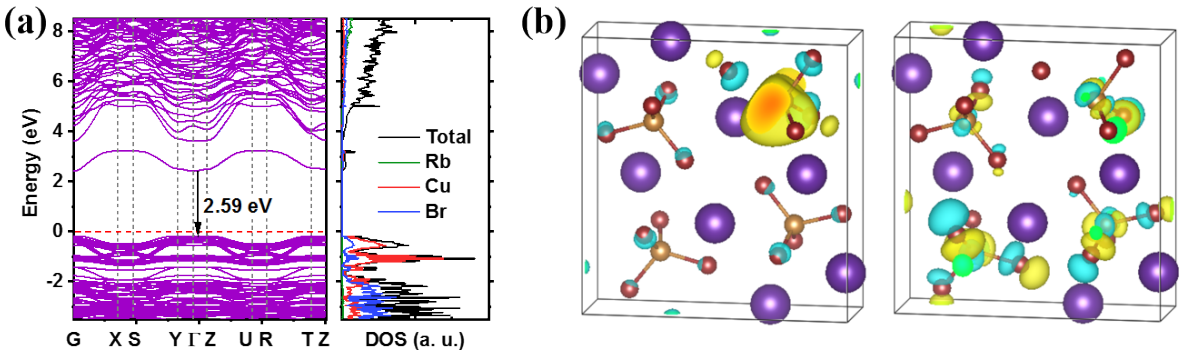

Figure S10. (a) The electronic band diagram, and (b) the electron wavefunctions at CBM and VBM after the formation of STE.

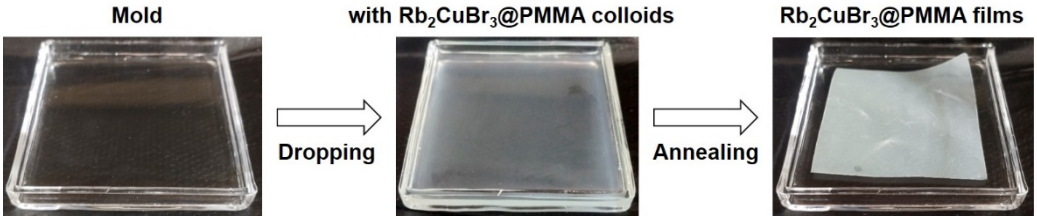

Figure S11. Fabrication process of Rb_2CuBr_3@PMMA composite film. Rb_2CuBr_3 NCs were mixed with PMMA colloids in a glass mold, subsequently followed by the degassing and curing processes at room temperature and in air for 2 h.

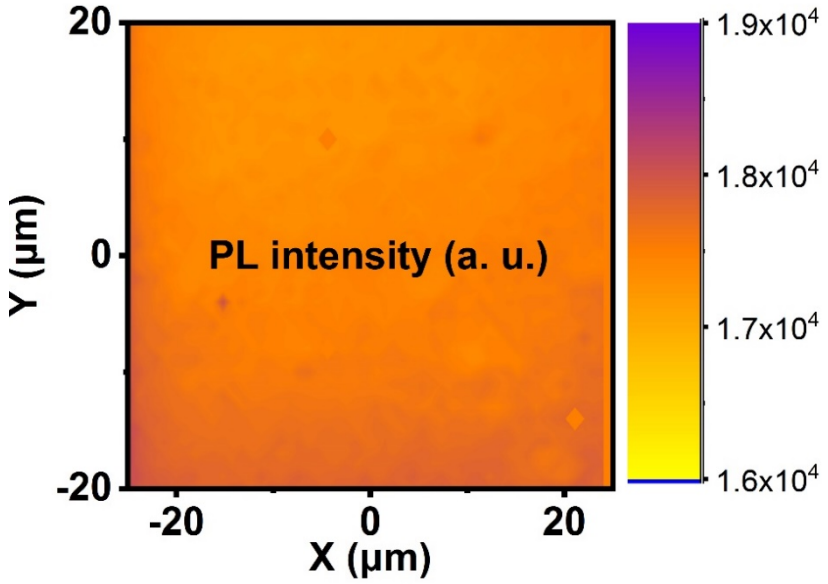

Figure S12. PL mapping of Rb_2CuBr_3@PMMA composite film.

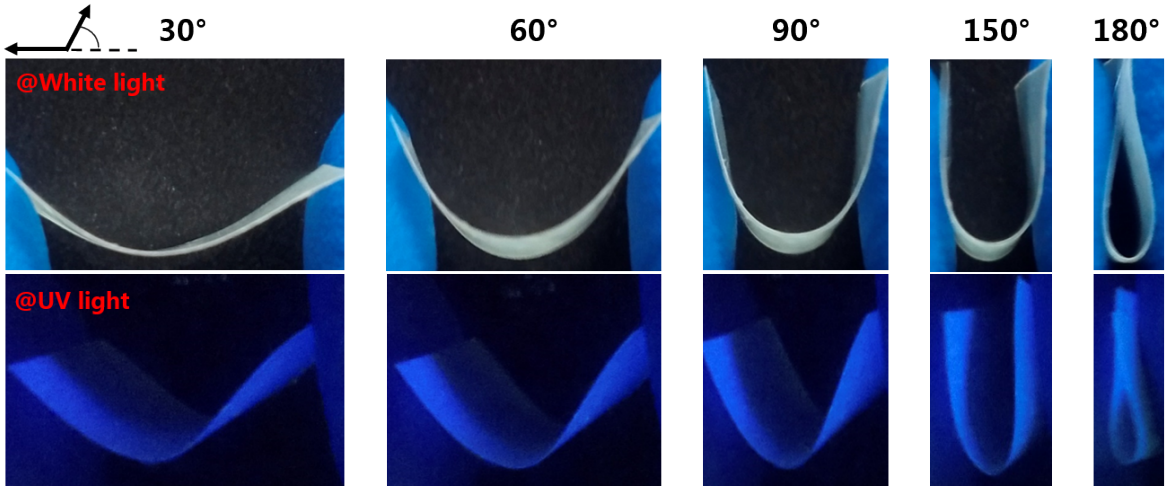

Figure S13. Flexbile Rb_2CuBr_3@PMMA films under white light and UV light illuminations.

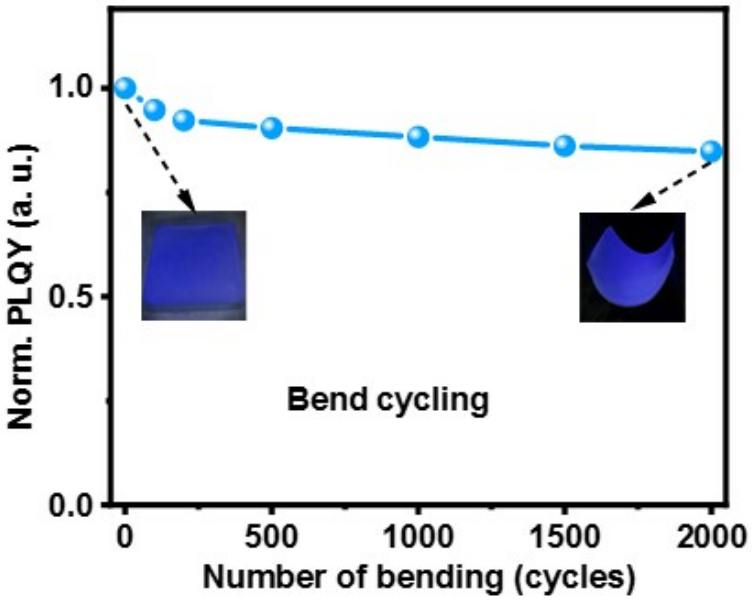

Figure S14. Normalized photoluminescence quantum yields (PLQYs) of Rb_2CuBr_3@PMMA films with increasing bending cycles.

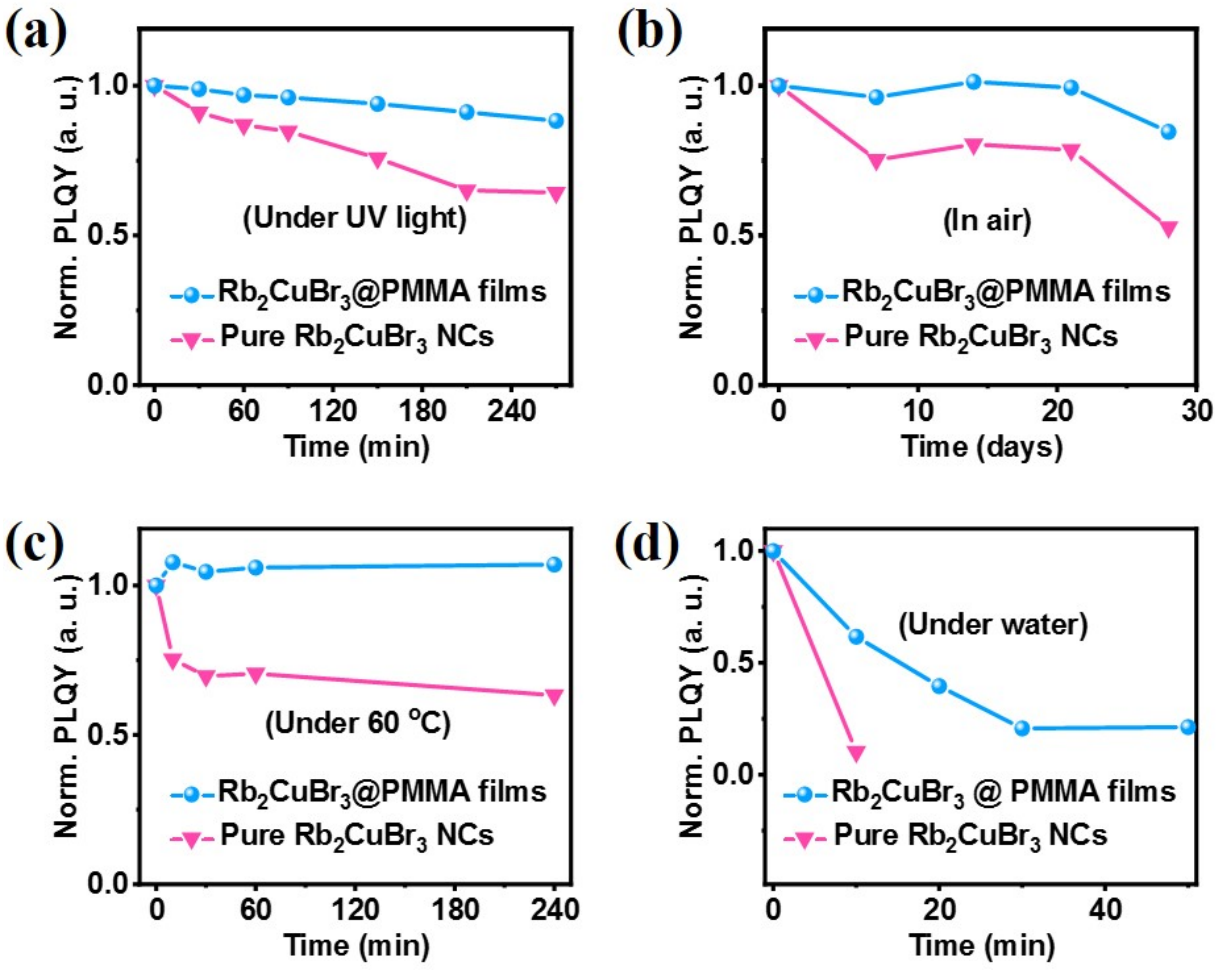

Figure S15. (a) and (b) The stability comparisons of the standalone Rb_2CuBr_3 NCs and Rb_2CuBr_3@PMMA films under continuous UV light irradiations and ambient environment exposure, respectively**.** (c) Normalized PLQYs of Rb_2CuBr_3 NCs and Rb_2CuBr_3@PMMA films after continuous heating (60 °C) for different time. The PLQY of Rb_2CuBr_3 NCs decreases after heating, which is due to the thermal quenching effect and agglomeration effect at high temperature. The PLQY of the Rb_2CuBr_3@PMMA films showed a slight increase after heating, which may be due to the evaporation of water from the sample surface. (d) Normalized PLQYs of Rb_2CuBr_3 NCs and Rb_2CuBr_3@PMMA films soaked in water for different time. The PLQY of Rb_2CuBr_3 NCs decreased rapidly after soaking in water, while the PLQY of Rb_2CuBr_3@PMMA films decreased slower, indicating that the polar solvent of water damages the samples greatly, and the polymer can slow this damage. This is because PMMA not only provides a matrix, but also effectively isolates water and oxygen in air.

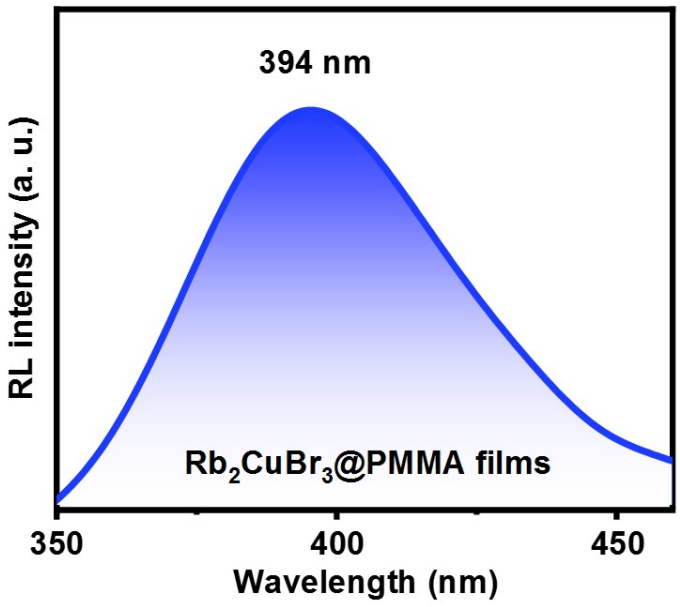

Figure S16. Radioluminescence (RL) spectra of Rb_2CuBr_3@PMMA films.

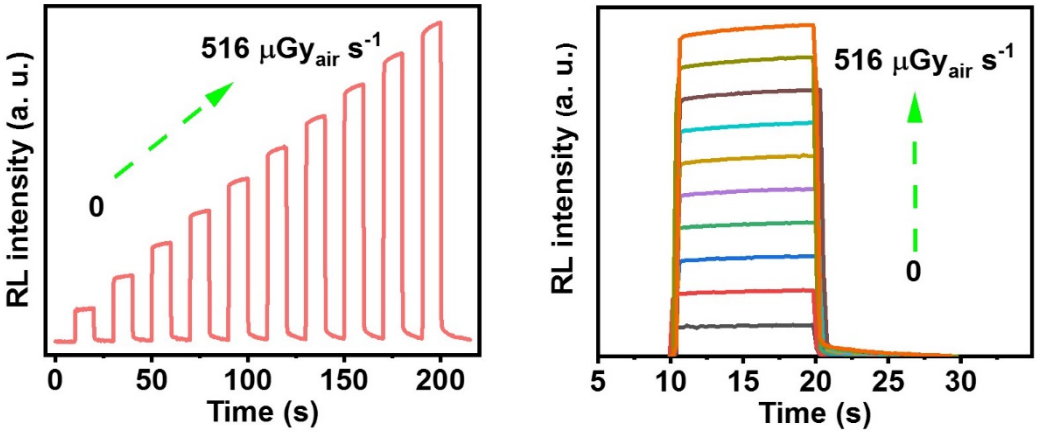

Figure S17. RL intensity-dose curve of Rb_2CuBr_3@PMMA films.

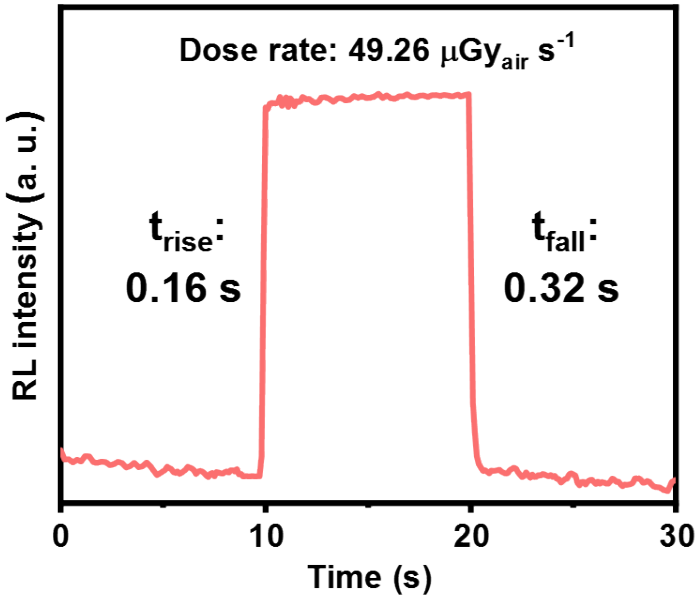

Figure S18. RL intensity-time curve of Rb_2CuBr_3@PMMA films.

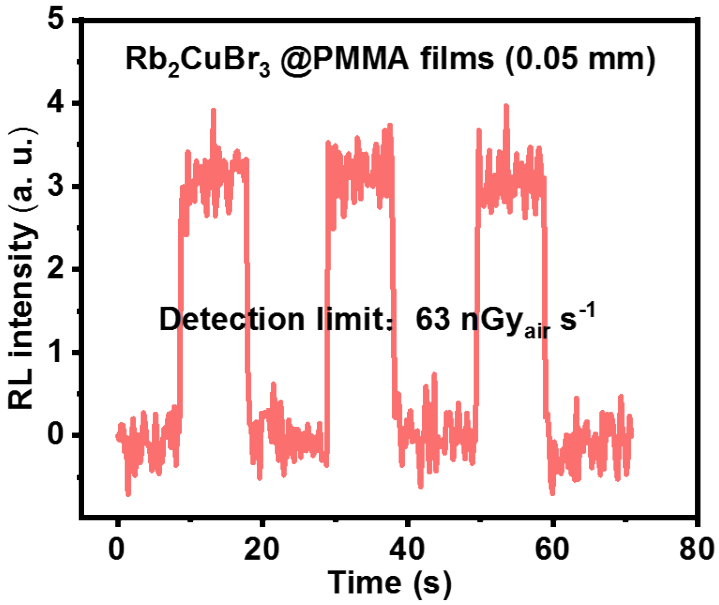

Figure S19. Detection limit of Rb_2CuBr_3@PMMA films (0.05 mm).

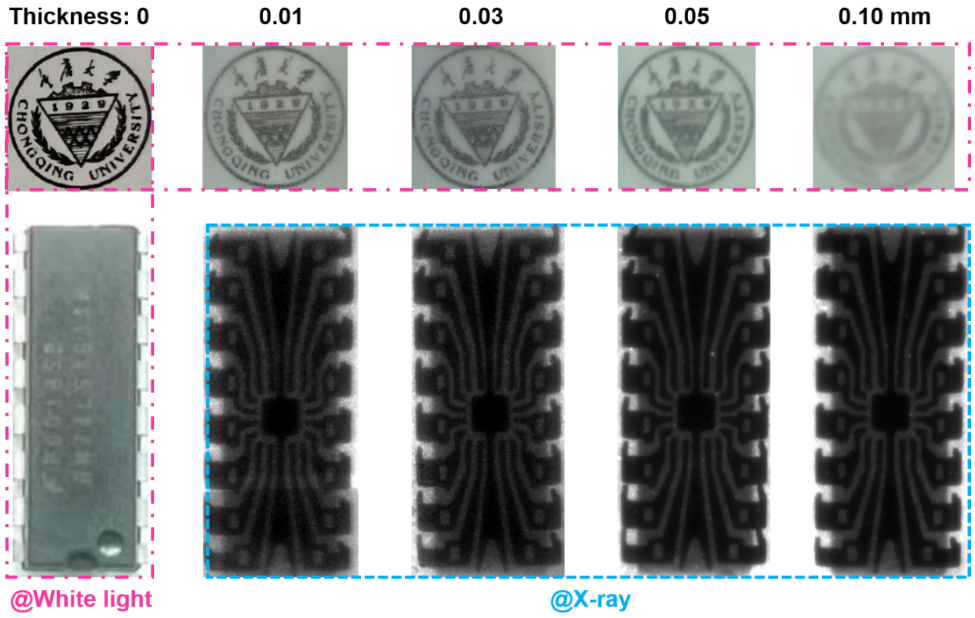

Figure S20. Upper panel: visible light transmission of Rb_2CuBr_3@PMMA films with different thickness as measured by covering the printed school badge by Rb_2CuBr_3@PMMA films. Lower panel: X-ray imaging of a chip under X-ray irradiation. Thicker films reduce the transmission rate of visible light, which may still be limited by the transparency of Rb_2CuBr_3 itself.

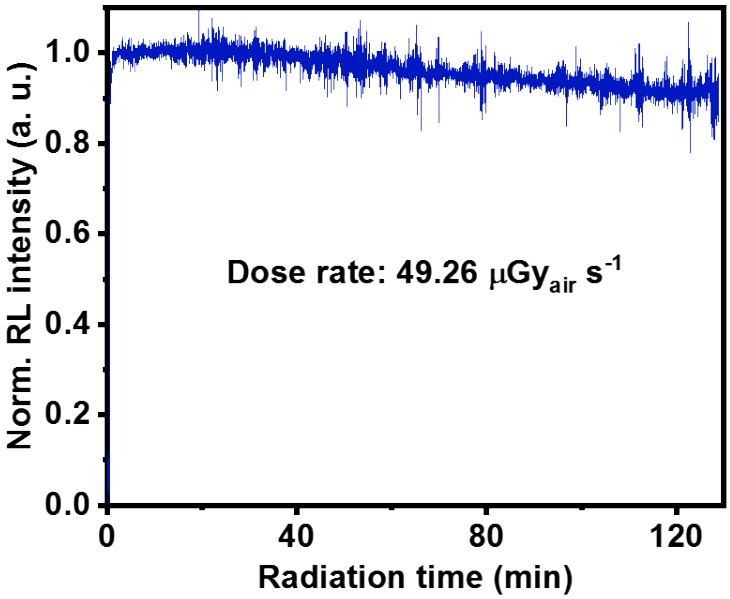

Figure S21. X-ray irradiation stability of Rb_2CuBr_3@PMMA films

Table S1. Performance comparisons of scintillators based on metal halide perovskites.

Chemical component	Flexible	Detection limit (nGy s^{-1})	Spatial resolution (lp mm^{-1})	Radiation stability (h)	Storage stability (h)	References
$CsPbBr_3$ NCs/MMA/ photoinitiator	Yes	-	9.8 (MTF=0.2)	-	-	[1]
$CsPbBr_3$ NCs/PDMS	Yes	13	5 (MTF=0.4)	35.3	-	[2]
$(C_8H_{17}NH_3)_2SnBr_4$/PMMA	Yes	-	2.5 (0.2 mm)	0.22		[3]
$(C_{38}H_{34}P_2)MnBr_4$ powder/PDMS	Yes	461.1	1.5 (0.322 mm)	4		[4]
$Cs_3Cu_2I_5$:Tl single crystals	No	66.3	-	-	-	[5]
$Cs_3Cu_2I_5$ powders/PDMS	Yes	-	6.8 (MTF=0.2)	1	~1440 (unchange in air)	[6]
$Cs_3Cu_2Cl_5$: 2% K^+/polystyrene	Yes	63.5	5			[7]
Rb_2CuCl_3 crystals	No	88.5	-	48 (>90%)	~1200 (>90% in air)	[8]
Rb_2CuBr_3 single crystal	No	121.5	-	-	1440 (in air)	[9]
Rb_2CuBr_3/polystyrene	Yes	-	1.7 (0.29 mm)	-	1008 (in air)	[10]
Rb_2CuBr_3 NCs/PMMA	**Yes**	**63**	**11.3 (MTF=0.2)**	**2.2**	**672 (>84% in air)**	**This work**

References

1. J. H. Heo, D. H. Shin, J. K. Park, D. H. Kim, S. J. Lee and S. H. Im, *Adv. Mater.*, 2018, **30**, 1801743.
2. Q. S. Chen, J. Wu, X. Y. Ou, B. L. Huang, J. Almutlaq, A. A. Zhumekenov, X. W. Guan, S. Y. Han, L. L. Liang, Z. G. Yi, J. Li, X. J. Xie, Y. Wang, Y. Li, D. Y. Fan, D. B. L. Teh, A. H. All, O. F. Mohammed, O. M. Bakr, T. Wu, M. Bettinelli, H. H. Yang, W. Huang and X. G. Liu, *Nature*, 2018, **561**, 88-93.
3. J. Cao, Z. Guo, S. Zhu, Y. Fu, H. Zhang, Q. Wang and Z. Gu, *ACS Appl. Mater. Interfaces*, 2020, **12**, 19797-19804.
4. L. J. Xu, X. S. Lin, Q. Q. He, M. Worku and B. W. Ma, *Nat. Commun.*, 2020, **11**, 4329.
5. S. L. Cheng, M. Nikl, A. Beitlerova, R. Kucerkova, X. Y. Du, G. D. Niu, Y. C. Jia, J. Tang, G. H. Ren and Y. T. Wu, *Adv. Opt. Mater.*, 2021, **9**, 2100460.
6. Y. C. Liu, Y. X. Zhang, Z. Yang, J. Cui, H. D. Wu, X. D. Ren, K. Zhao, J. S. Feng, J. Tang, Z. Xu and S. Z. Liu, *Adv. Opt. Mater.*, 2020, **8**, 2000814.
7. L. L. Han, B. B. Sun, C. Guo, G. Q. Peng, H. Y. Chen, Z. Yang, N. Li, Z. P. Ci and Z. W. Jin, *Adv. Opt. Mater.*, 2022, **10**, 2102453.
8. X. Zhao, G. D. Niu, J. S. Zhu, B. Yang, J. H. Yuan, S. R. Li, W. R. Gao, Q. S. Hu, L. X. Yin, K. H. Xue, E. Lifshitz, X. S. Miao and J. Tang, *J. Phys. Chem. Lett.*, 2020, **11**, 1873-1880.
9. B. Yang, L. Yin, G. Niu, J. H. Yuan, K. H. Xue, Z. Tan, X. S. Miao, M. Niu, X. Du, H. Song, E. Lifshitz and J. Tang, *Adv Mater*, 2019, **31**, e1904711.
10. L. L. Han, H. Zhang, Y. Y. Ning, H. Y. Chen, C. Guo, J. H. Cui, G. Q. Peng, Z. P. Ci and Z. W. Jin, *Chem. Eng. J.*, 2022, **430**, 132826.